Antibody-functionalized nanoparticles for imaging cancer: influence of conjugation to gold nanoparticles on the biodistribution of ^{89}Zr-labeled cetuximab in mice

Linda Karmani[a], Daniel Labar[b], Vanessa Valembois[c], Virginie Bouchat[c], Praveen Ganesh Nagaswaran[d], Anne Bol[b], Jacques Gillart[b], Philippe Levêque[a], Caroline Bouzin[e], Davide Bonifazi[d], Carine Michiels[f], Olivier Feron[e], Vincent Grégoire[b], Stéphane Lucas[c], Thierry Vander Borght[b] and Bernard Gallez[a]*

Antibody-labeled gold nanoparticles represent a promising novel tool regarding cancer imaging and therapy. Nevertheless, the characterization of biodistribution of such immunonanocarriers has been poorly documented. In this study, the biodistribution of ^{89}Zr-labeled cetuximab before and after the coupling reaction to gold nanoparticles (AuNPs) was compared and the quantitative imaging performance of ^{89}Zr immuno-PET was evaluated. Cetuximab was functionalized with the desferal moiety and labeled with ^{89}Zr (^{89}Zr–Df–Bz–NCS–cetuximab). AuNPs with a mean diameter of 5 nm were synthesized according a new method developed in the laboratory, and conjugated to ^{89}Zr–Df–Bz–NCS–cetuximab using carbodiimide chemistry (AuNPs–PPAA–cetuximab–^{89}Zr). The two tracers were injected in A431 xenograft-bearing mice. Tumor and liver uptakes were assessed at different times after injection using quantitative PET imaging. The *in vivo* specificity of the binding was investigated using a saturating dose of unlabeled cetuximab. Radiolabeled cetuximab was conjugated to AuNPs with a coupling reaction yield >75%. All conjugates were stable *in vitro* and to a lesser extent in plasma. *In vivo* distribution studies revealed no significant difference in tumor uptake for cetuximab conjugated to nanoparticles up to 72 h after injection, compared with unconjugated cetuximab. Immuno-PET studies showed that AuNPs–PPAA–cetuximab–^{89}Zr provided high tumor-to-background ratio. The liver uptake of AuNPs–PPAA–cetuximab–^{89}Zr was higher, compared with ^{89}Zr–Df–Bz–NCS–cetuximab. *In vivo* blocking experiments demonstrated selective tumor targeting after coupling reaction. This study showed that the conjugation of AuNPs to cetuximab did not affect its tumor accumulation and that the efficacy of EGFR-targeted nanoparticles was unaltered. The ^{89}Zr-labeled cetuximab-targeted gold nanoparticles could be a valuable tool for theranostic purposes. Copyright © 2013 John Wiley & Sons, Ltd.
Supporting information may be found in the online version of this paper.

Keywords: immuno-PET; EGFR; ^{89}Zr; cetuximab-targeted gold nanoparticles; molecular imaging

1. INTRODUCTION

The emerging nanomedicines provide attractive tools that have a potential to improve cancer detection and therapy efficiency (1).

Gold nanoparticles (AuNPs) are known for their good biocompatibility profiles and their interesting properties. Owing to their optical absorption properties, gold nanoparticles have shown potential as contrast agents for optoacoustic cancer imaging (2)

* Correspondence to: B. Gallez, Biomedical Magnetic Resonance Group, Louvain Drug Research Institute, Université Catholique de Louvain, Avenue Mounier 73, 1200 Brussels, Belgium. E-mail: Bernard.Gallez@uclouvain.be

a L. Karmani, P. Levêque, B. Gallez
  Biomedical Magnetic Resonance Group, Louvain Drug Research Institute, Université Catholique de Louvain, Avenue Mounier 73, 1200, Brussels, Belgium

b D. Labar, A. Bol, J. Gillart, V. Grégoire, T. V. Borght
  Center for Molecular Imaging, Radiotherapy and Oncology, Institute of Experimental and Clinical Research, Université Catholique de Louvain, Avenue Hippocrate 54, 1200, Brussels, Belgium

c V. Valembois, V. Bouchat, S. Lucas
  Research Center for the Physics of Matter and Radiation, University of Namur,

Namur Research Institute for Life Sciences, Rue de Bruxelles 61, 5000, Namur, Belgium

d P. G. Nagaswaran, D. Bonifazi
  Namur Research College and Department of Chemistry, University of Namur, Rue de Bruxelles 61, 5000, Namur, Belgium

e C. Bouzin, O. Feron
  Pole of Pharmacology and Therapeutics, Institute of Experimental and Clinical Research, Université Catholique de Louvain, Avenue Mounier 53, 1200, Brussels, Belgium

f C. Michiels
  Unité de Recherche en Biologie Cellulaire, University of Namur, Namur Research Institute for Life Sciences, Rue de Bruxelles 61, 5000, Namur, Belgium

and can be used as photothermal agents in cancer therapy (3). However, their small size facilitates their entry into various cells and makes it difficult to use them for targeted delivery to specific tissues. Development of active targeting of nanoparticles, such as nanoparticle conjugation to tumor-specific ligands, may constitute the next generation of polymeric nanoparticles drug delivery systems and would be a solution to improve targeted delivery (4). The active targeting involves the incorporation of molecules that specifically bind an antigen or receptor that is either exclusively expressed or overexpressed on the tumor cell surface. Monoclonal antibodies (mAbs) have long been considered as interesting candidates for targeted cancer therapy and diagnostics, thanks to their highly specific targeting ability. Although antibodies are used successfully as intrinsic therapeutic agents, they have also the ability to be exploited as targeting agents (5). The antibody-targeted nanoparticles were expected as a strategy to enhance the efficacy of tumor targeting for nanoparticle delivery systems while reducing toxicity in normal tissues (4). To functionalize gold nanoparticles we have chosen cetuximab, a mouse–human chimeric monoclonal antibody that binds competitively and with high affinity to the epidermal growth factor receptor (EGFR). The EGFR is an attractive target for anticancer therapy (6) as this tyrosine kinase receptor is overexpressed in many epithelial solid tumors. Currently, cetuximab (Erbitux®) is approved for the treatment of metastatic colorectal cancer and has been shown to inhibit ligand binding, receptor dimerization and downstream signaling by binding to extracellular domain of the EGFR (7). Several antibody-based strategies have been developed to block EGFR activation and are used clinically (8,9). Moreover, EGFR targeting has also been achieved using several immunoconjugates including cetuximab conjugated to gold nanoparticles (10–13).

Many studies have described the biological distribution of nanoparticles according to their size, shape, surface charge, mechanical properties and chemistry, as well as the route of administration (14), but few reports are available on biodistribution experiments with antibody-functionalized nanoparticles (15). For this purpose, we studied the impact of cetuximab conjugation to gold nanoparticles on their in vivo distribution behavior compared with unconjugated antibody. To trace these immunoconjugates, cetuximab was previously radiolabeled using zirconium-89 (^{89}Zr). ^{89}Zr is a promising candidate for positron emission tomography (PET) (16). Immuno-PET using ^{89}Zr has been particularly applied in cancer research. In addition to numerous animal studies (17,18), the application of ^{89}Zr-labeled antibodies to detect primary tumors in human has been successfully demonstrated in several studies (19,20). In fact, antibody-based radiotracers require extended in vivo circulation times for optimal biodistribution and tumor targeting (21). Therefore, the long physical half-life of ^{89}Zr (78.41 h) is compatible with the time needed for most intact antibodies to achieve optimal tumor-to-nontumor ratio (typically 2–4 days). In the current study, we used the labeling of cetuximab with ^{89}Zr and animal PET imaging to monitor the influence of gold nanoparticles conjugation on the biological distribution of the antibody.

2. RESULTS AND DISCUSSION

2.1. Characterization of ^{89}Zr-labeled cetuximab and ^{89}Zr-cetuximab conjugated to AuNPs

Radiolabeling of Df–Bz–NCS-cetuximab with ^{89}Zr-oxalate was achieved with a mean radiochemical yield of 30% (n = 6),

whereas the radiochemical purity immediately after purification was >95% (n = 6). The resulting specific activity was 50.9 ± 9.8 MBq mg^{-1} of mAb (n = 6). Electrophoresis of ^{89}Zr-labeled Df–Bz–NCS-cetuximab under nonreducing conditions followed by radio-TLC and autoradiography showed a single band of 150 kDa corresponding to ^{89}Zr–Df–Bz–NCS–cetuximab and a single peak of radioactivity (see supplementary figure 1a in the online Supporting Information), which means that antibody integrity remained preserved after labeling reaction.

After coating nanoparticles with PPAA (plasma-polymerized allylamine), the nanoparticle diameters observed by transmission electron microscopy (TEM) imaging ranged from 3 to 10 nm (mean diameter of 4.8 ± 1.7 nm) (22). The mean diameter of cetuximab after coupling to gold nanoparticles was determined by CPS disk centrifuge and was estimated about 31.0 ± 10.4 nm (see supplementary figure 2 in the online Supporting Information). Electrophoresis of cetuximab-labeled gold nanoparticles under nonreducing conditions followed by radio-TLC showed a lower migration of AuNPs–PPAA–cetuximab–^{89}Zr compared with ^{89}Zr–Df–Bz–NCS–cetuximab and two peaks of radioactivity corresponding to the position of the two species on the gel (see supplementary figure 1b in the online Supporting Information). The percentage of radioactivity linked to the peak of AuNPs–PPAA–cetuximab–^{89}Zr expressed the coupling reaction yield, which was greater than 75% (n = 3). In order to enhance the coupling yield, the coupling reaction was achieved overnight. This conjugation step is quite long and inconvenient for possible future theranostic use of these nanoconjugates. The coupling reaction of antibodies to gold nanoparticles could be optimized for later studies by using another cross-linking method like click chemistry. The modern click chemistry method is known for its high coupling efficiency and shorter time of reaction compared with conventional carbodiimide chemistry (23). Thermogravimetric analysis revealed the number of coupled antibodies molecules per nanoparticle, which was estimated to be 5–10 mAbs per nanoparticle (22). Finally, a cell-based ELISA, phosphorylation assays and subsequent western blot analysis showed that the in vitro binding activity of cetuximab after coupling reaction to nanoparticles was quantitatively slightly reduced compared with uncoupled cetuximab but qualitatively preserved (22).

2.2. PET evaluation of ^{89}Zr-labeled cetuximab biodistribution in mice before and after coupling reaction to AuNPs

Two groups of A431 bearing nude mice were injected with ^{89}Zr–Df–Bz–NCS–cetuximab or AuNPs–PPAA–cetuximab–^{89}Zr, respectively. We compared the pharmacokinetic behavior of AuNPs–PPAA–cetuximab–^{89}Zr with that of ^{89}Zr–Df–Bz–NCS–cetuximab, as a reference compound. Figure 1 shows representative PET images of A431 xenograft bearing nude mice at 48 h after tracer injection, and compares the distributions of ^{89}Zr–Df–Bz–NCS–cetuximab (Fig. 1a) and AuNPs–PPAA–cetuximab–^{89}Zr (Fig. 1b). The accumulation of the two tracers was most predominantly observed in the liver (red arrows) and in tumors implanted in both legs (green arrows). For both radioimmunoconjugates, a similar pattern was observed, but with a higher liver and spleen uptake for AuNPs–PPAA–cetuximab–^{89}Zr. This distribution pattern remained constant at later time points (data not shown). 3D videos related to PET study are available online as supplementary materials 3 and 4 for ^{89}Zr–Df–Bz–NCS–cetuximab and AuNPs–PPAA–cetuximab–^{89}Zr respectively (Supporting Information).

In the tumor, the kinetics were slow for both coupled and uncoupled ^{89}Zr-labeled cetuximab (Fig. 2a), with a maximum uptake reached
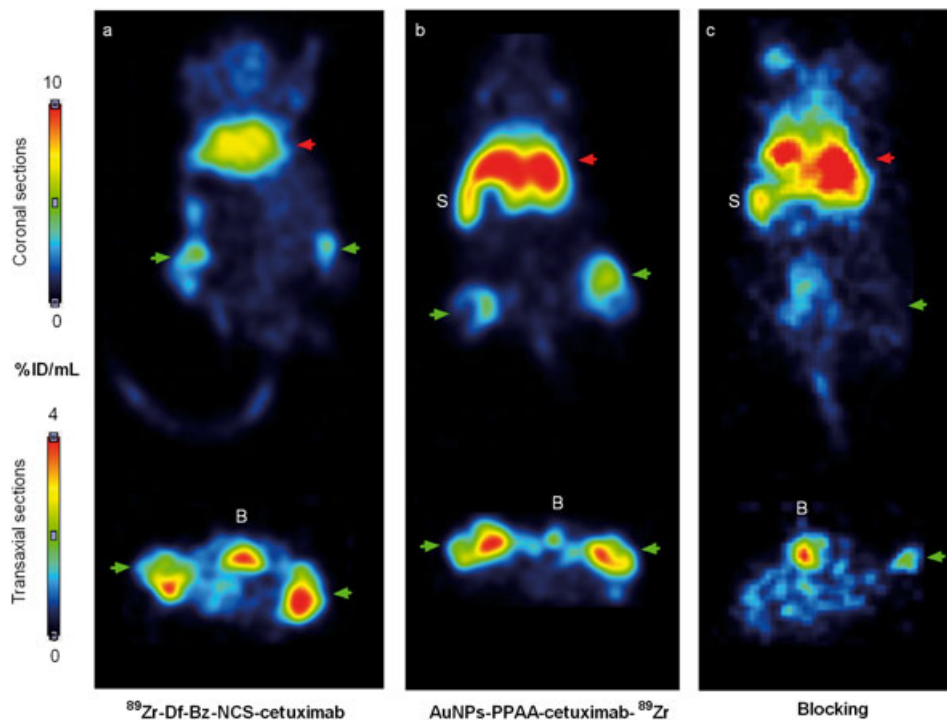
Figure 1. A431-bearing nude mice, injected with ^{89}Zr–Df–Bz–NCS–cetuximab (a) or AuNPs–PPAA–cetuximab–^{89}Zr (b) (two tumors per mouse), or AuNPs–PPAA–cetuximab–^{89}Zr 2 h after a blocking dose of unlabeled cetuximab (c) (one tumor per mouse). Coronal (upper) and transaxial (lower) PET images were obtained 48 h after injection. Color scales, expressed as %ID ml^{-1}, indicate radioactivity uptake levels in tumors (green arrows) and in liver (red arrows). The bladder is indicated with 'B' and the spleen with 'S'.
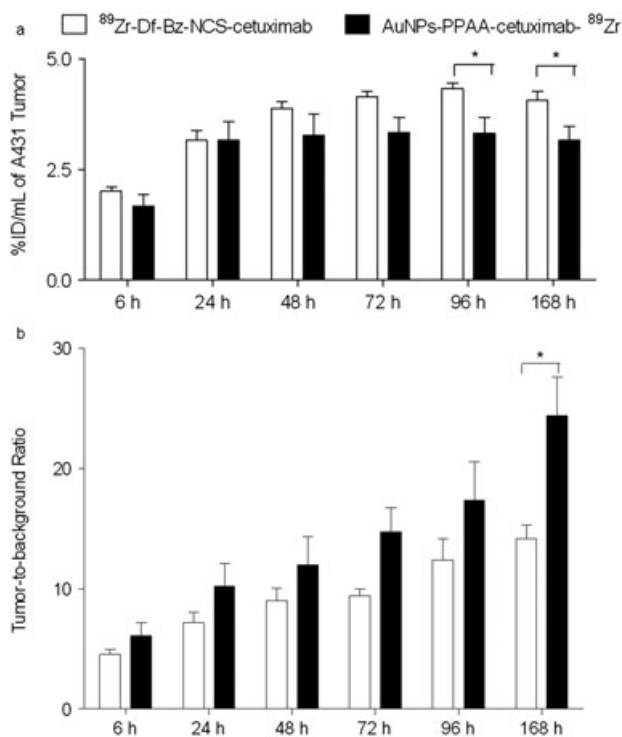

Figure 2. Tumor uptake (a) and tumor-to-background ratio (b) of ^{89}Zr–Df–Bz–NCS–cetuximab (white bars) or AuNPs–PPAA–cetuximab–^{89}Zr (black bars) in A431-bearing nude mice at 6, 24, 48, 72, 96 and 168 h after injection. Injected activity ranged from 3.3 to 4.6 MBq, corresponding to a total of 200–350 μg mAb per mouse. Results are expressed as means $\pm$ SEM ($n = 3$–5). * $p < 0.05$.

after 48 h and followed by a plateau phase (3.9 ± 0.1 for ^{89}Zr–Df–Bz–NCS–cetuximab and 3.3 ± 0.5 for AuNPs–PPAA–cetuximab–^{89}Zr). No difference in tumor uptake between the two groups was seen at early time points. A small, statistically significant difference of uptake was noted at 96 and 168 h. In terms of tumor-to-background ratio, a continuous increase was observed over time, with no difference between the two groups except for the latest time point (168 h) in favor of AuNPs–PPAA–cetuximab–^{89}Zr (Fig. 2b). This trend suggested a lower background for mice receiving antibody conjugated to gold nanoparticles, which would probably be related to the more important tracer uptake by the reticuloendothelial system and particularly by the liver. Thus, we demonstrated that the tumor uptake of the vectorized gold nanoparticles was mostly similar to that of uncoupled cetuximab. A small difference could only be seen for late time points, the tumor uptake being then slightly lower for the AuNPs–PPAA–cetuximab–^{89}Zr when expressed as percentage of the injected dose per milliliter (%ID ml^{-1}), but higher when expressed as tumor-to-background ratio. The preservation of high tumor contrast after nanoparticle conjugation, expressed as tumor-to-background ratio, supports the good imaging properties of AuNPs–PPAA–cetuximab–^{89}Zr.

Major differences between both biodistribution patterns were observed for liver and spleen uptake (Fig. 1). For each time point considered, it must be mentioned that the liver uptake for AuNPs–PPAA–cetuximab–^{89}Zr was quite important, more than twice as that of the unconjugated cetuximab (Fig. 3). The uptake by the liver was fast and the maximum uptake value was reached at 6 h after tracer injection (13.4 ± 0.6 for AuNPs–PPAA–cetuximab–^{89}Zr and 7.5 ± 0.3 for ^{89}Zr–Df–Bz–NCS–cetuximab). One of the limitations of antibody-based imaging is the high background signal in the reticuloendothelial system, which was particularly
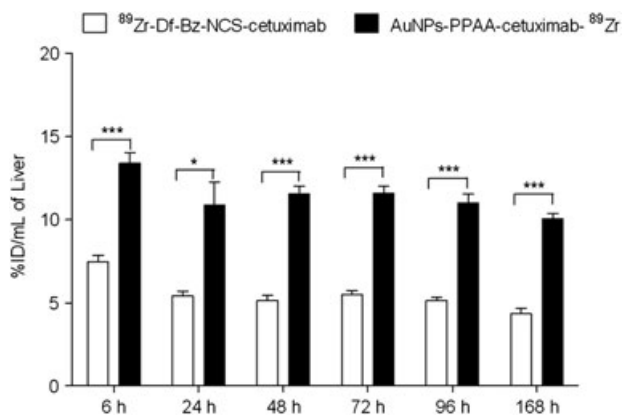
Figure 3. Liver uptake of ^{89}Zr-Df-Bz-NCS-cetuximab (white bars) or AuNPs-PPAA-cetuximab-^{89}Zr (black bars) in A431 bearing nude mice at 6, 24, 48, 72, 96 and 168 h after injection. Injected activity ranged from 3.3–4.6 MBq corresponding to a total of 200–350 µg mAb per mouse. Results are expressed as means ± SEM (n = 3–5). * $p < 0.05$; *** $p < 0.0001$.

illustrated in our study by liver uptake of ^{89}Zr–Df–Bz–NCS–cetuximab. Moreover, the colloidal properties of gold nanoparticles could be the cause of the enhanced AuNPs–PPAA–cetuximab–^{89}Zr accumulation in the reticuloendothelial system.

The specificity of tumor uptake was investigated by administering a saturating dose of unlabeled cetuximab 2 h before AuNPs–PPAA–cetuximab–^{89}Zr injection. In this saturation experiment, the binding of AuNPs–PPAA–cetuximab–^{89}Zr was markedly reduced in the tumor, as illustrated on images obtained 48 h after injection of the tracer (Fig. 1c). The residual activity in the tumor was significantly lower for the blocking group at each time point compared with tumor uptake in mice injected with only AuNPs–PPAA–cetuximab–^{89}Zr (Fig. 4a). In fact, the tumor uptake value in the blocking group (1.5 ± 0.1 %ID ml^{-1}) was reduced by a factor of 2.2 at 48 h after injection compared with mice receiving only AuNPs–PPAA–cetuximab–^{89}Zr (3.3 ± 0.5 % ID ml^{-1}). In terms of tumor-to-background ratio, the reduction in tumor uptake for the blocking group was more pronounced and was significant at each time point, compared with the nonsaturating group (Fig. 4b). Indeed, the tumor-to-background ratio value was equal to 3.4 ± 0.5 for the blocking group and 12.0 ± 2.3 for mice receiving only AuNPs–PPAA–cetuximab–^{89}Zr, at 48 h after injection. We demonstrated that administration of unlabeled antibodies in excess before AuNPs–PPAA–cetuximab–^{89}Zr injection induced the saturation of EGFR binding sites and decreased significantly the EGFR-binding of AuNPs–PPAA–cetuximab–^{89}Zr in tumors. These results suggested the selective accumulation and the EGFR-specific binding of AuNPs–PPAA–cetuximab–^{89}Zr *in vivo*. It also confirmed the preservation of the EGFR recognition by the antibody after its radiolabeling and coupling to nanoparticles in agreement with previous *in vitro* studies showing its preservation after chelation and radiolabeling (24,25). Indeed, the functionalization of cetuximab with a three-fold molar excess of Df–Bz–NCS led to a reproducible chelate:mAb substitution ratio of 1.5:1. Such a low chelate–mAb ratio was reported not to alter the pharmacokinetic nor the immunoreactivity of the antibody. In addition, our previous studies showed that the *in vitro* binding activity of AuNPs–PPAA–cetuximab–^{89}Zr (EC_{50} 0.08 µg ml^{-1}) remained in the same range as for ^{89}Zr–Df–Bz–NCS–cetuximab (EC_{50} 0.19 µg ml^{-1}) (22).

Finally, it can also be emphasized that we did not observe radioactivity accumulation in other nonspecific organs, apart from
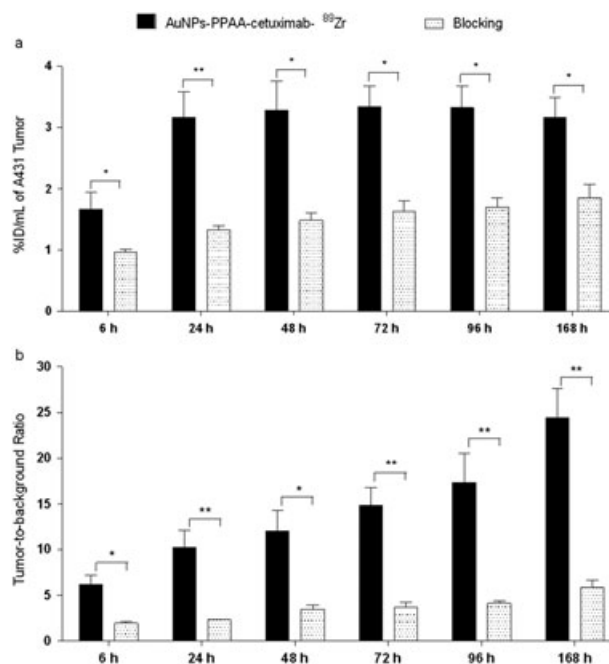

Figure 4. Tumor uptake (a) and tumor-to-background ratio (b) of AuNPs–PPAA–cetuximab–^{89}Zr (3.3–4.6 MBq, total of 200–350 µg mAb per mouse) or AuNPs–PPAA–cetuximab–^{89}Zr (2.2–3.5 MBq, total of 200 µg mAb per mouse) after a blocking dose of unlabeled cetuximab (2000 µg mAb per mouse) in A431-bearing nude mice at 6, 24, 48, 72, 96 and 168 h after injection. Results are expressed as means ± SEM (n = 3). * $p < 0.05$; ** $p < 0.01$.

liver, spleen and bones. For the two groups of mice and starting from 24 h after injection, the maximum intensity projection images showed an accumulation of radioactivity in bones, which was particularly enhanced at 48 h after injection (Fig. 5). PET images displayed distinct hot spots in joints (shoulders and knees) and in the whole mouse backbone. A similar pattern of skeleton uptake was also reported for ^{89}Zr-labeled trastuzumab (26). The bone uptake might be assigned to the detachment of ^{89}Zr from
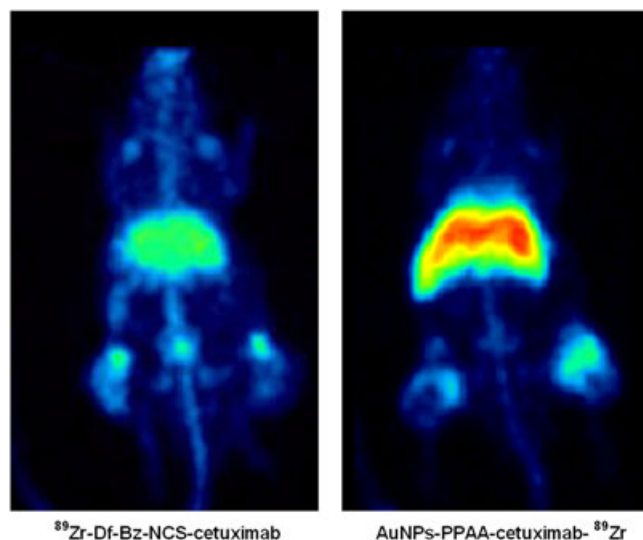

Figure 5. Maximum intensity projection of ^{89}Zr–Df–Bz–NCS–cetuximab (left) and AuNPs–PPAAcetuximab–^{89}Zr (right) 48 h after injection in A431-bearing nude mice (two tumors per mouse). Upper and lower intensity threshold were set at 100% and 0% respectively.

the desferal moiety. First, we observed that the two tracers were not fully stable in physiological conditions, a release of free [89]Zr being observed up to 10% after 24 h of plasmatic *in vitro* incubation. Second, previous studies attributed constant bone accumulation to the strong affinity of free [89]Zr[4+] for hydroxylapatite and phosphate constituents of bones. In fact, zirconium is known to bind to plasma proteins and it is later deposited in mineral bone (27). Other studies hypothesized that high murine bone uptake is also due to the liver metabolism of the conjugate and the release of free [89]Zr into the circulation (28).

3. CONCLUSIONS

Development of more efficient drug delivery systems is important to effectively target cancer cells. Gold nanoparticles, used as scaffolds to which antibodies are attached, were previously described as valuable tools for imaging and/or treating cancers. Nevertheless, the characterization of *in vivo* distribution of such scaffolds was poorly documented. Because our group has recently developed a method to synthesize gold nanoparticles (29), we addressed in this work the question of the nanoparticle vectorization through conjugation to cetuximab, a specific monoclonal antibody directed against EGFR. We combined the targeting properties of cetuximab and favorable imaging properties of [89]Zr to further characterize the *in vivo* behaviour of these vectorized nanoparticles and the *in vivo* impact of nanoparticle conjugation on antibody distribution by using noninvasive PET imaging.

We demonstrated that the conjugation of cetuximab to gold nanoparticles does not significantly affect the EGFR-dependent tumor uptake in mice. However, the reticuloendothelial system uptake of [89]Zr-labeled cetuximab conjugated to gold nanoparticles was higher than for [89]Zr-labeled antibody alone. This could be a limitation for the use of radioactive nanoparticles for systemic metabolic radiotherapy, but not for strategies based on photothermal therapy where nanoparticle activation can be controlled. Overall, PET-imaging using [89]Zr-labeled antibodies is a powerful tool to analyse the *in vivo* properties of complex systems like immunonanocarriers suggested for theranostic applications and more specifically for photodynamic therapy, which is an attractive alternative to surgery or radiation for the management of malignant tumors.

4. EXPERIMENTAL

4.1. Production and purification of [89]Zr

[89]Zr was produced and purified as previously described (30,31). In brief, [89]Zr was produced in-house via a (p,n) reaction on natural yttrium ([89]Y) using a Cyclone® 30 cyclotron (IBA, Louvain-la-Neuve, Belgium). For this purpose, 100 mg of 100% ([89]Y)-Y$_2$O$_3$ powder (Sigma-Aldrich, Belgium, 99.99% purity) was bombarded with incident proton-beam ($E_p = 14$ MeV, 10 µA) for about 10 h.

The irradiated [89]Y target was dissolved in 6 mol l^{-1} HCl (Sigma-Aldrich, Belgium) at 120 °C for 30 min, then diluted with water (>18 MΩ cm^{-1}, 25 °C, Milli-Q, Millipore) to ensure a final concentration of 2 mol l^{-1} HCl. The obtained solution was loaded onto a solid-phase hydroxamate column (100 mg), which was prepared as previously reported (30,32). The column was washed with 2 mol l^{-1} HCl and Milli-Q water, respectively, to remove [89]Y ions and other radionuclidic metal impurities. [89]Zr was finally slowly eluted with 1 mol l^{-1} oxalic acid (Sigma-Aldrich, 99.999% purity). All used reagents and solvents were of trace analysis quality.

4.2. Preparation and characterization of [89]Zr-labeled cetuximab

[89]Zr–Df–Bz–NCS–cetuximab was prepared according to a protocol previously described (33,34). First, cetuximab (Erbitux® 5 mg ml^{-1}, Merck, Belgium) was purified by discontinuous filtration in centrifugal filter device with a molecular weight cut-off of 10 kDa (Vivaspin, Sartorius, Belgium). Then, the purified cetuximab was functionalized with the bifunctional chelating agent *p*-isothiocyanatobenzyl-desferrioxamine (Df–Bz–NCS, Macrocyclics, Dallas, TX, USA). In short, a three-fold molar excess of Df–Bz–NCS in 20 µl DMSO (Sigma-Aldrich, Belgium) was added to the antibody solution (2 mg in 1 ml 0.1 M NaHCO$_3$ buffer, pH 9.0) and incubated for 30 min at 37 °C. The isothiocyanate group of the chelate agent forms a thiourea bond with a primary amine of the antibody lysine groups. Finally, the functionalized cetuximab (Df–Bz–NCS-cetuximab) was purified by size exclusion chromatography using a PD10 column (GE Healthcare Life Sciences, Belgium) and radiolabeled with produced [89]Zr (111 MBq) at room temperature for 60 min, followed by gel filtration purification using 5 mg ml^{-1} gentisic acid in 0.25 M sodium acetate (pH 5.4–5.6) as mobile phase. During the critical steps of the antibody functionalization and radiolabeling, the pH was carefully adjusted with a pH meter (Inolab®, pH 730, WTW) equipped with a micro pH electrode (Inlab® Micro, Mettler Toledo).

The radiochemical yield and purity were determined using instant thin-layer chromatography (ITLC) and 20 mM citric acid (pH 4.9–5.1) as mobile phase. ITLC migration was followed by radio-TLC detection (Mini-Gita TLC scanner, Raytest, Germany) and showed that the radiolabeled antibody migrated with $R_f < 0.1$, whereas unbound [89]Zr migrated to the solvent front (R_f is the distance that compound has traveled divided by the distance that the solvent has traveled). In addition, the integrity of the antibody after radiolabeling was checked using sodium dodecyl sulfate–polyacrylamide gel electrophoresis (10% SDS–PAGE gel, under nonreducing conditions), followed by radio-TLC detection (Bioscan system 200 imaging scanner), and by scanning gel using Phosphor Imager (Fujifilm FLA-5100) analysis.

4.3. Synthesis and characterization of [89]Zr-labeled cetuximab and conjugated to AuNPs

The gold nanoparticles were synthesized and coated with PPAA by physical vapour deposition as previously described by our group (29). The coated nanoparticles (AuNPs–PPAA) were purified by discontinuous filtration in centrifugal filter device with a molecular weight cut-off of 10 kDa. Cetuximab was then coupled to coated nanoparticles using carbodiimide chemistry, as recently described (35). In summary, the amino groups present in the polymeric coating of AuNPs–PPAA were exploited to form an amide bond with the carboxyl groups of the antibody. About 1 mg of [89]Zr–Df–Bz–NCS–cetuximab was added in 5 ml of an aqueous solution containing 95 mg of 2-(N-morpholino)ethanesulphonic acid hydrate (Sigma-Aldrich, Belgium), 1 mg of N-hydroxy-sulphosuccinimide (Sigma-Aldrich, Belgium) and 1 mg of 3-carbodiimide hydrochloride (Sigma-Aldrich, Belgium). The mixture was stirred for 20 min at 25 °C, after which the aqueous solution of AuNPs–PPAA (1.3 mg, 2 ml) was added. The reaction was stirred at 25 °C for a period of 16 h. The [89]Zr-labeled antibodies conjugated to nanoparticles (AuNPs–PPAA–cetuximab–[89]Zr) were purified by filtration, using membrane filter of molecular weight cut-off of 300 kDa (Millipore, Belgium).

Transmission electron microscopy (Philips Tecnai 10 transmission electron microscope) was carried out to assess the morphology

and size distribution of AuNPs–PPAA as previously described (35). Differential centrifugal sedimentation (DC 24000 Disc Centrifuge; CPS Instruments Inc.) was achieved to determine the size of AuNPs–PPAA–cetuximab–^{89}Zr by measuring the time required for the radioimmunoconjugates to traverse a sucrose density gradient created in a disk centrifuge. This method uses calibrated gold nanoparticles coated layer-by-layer with polyelectrolytes to estimate the size of the tracer (35). The efficiency of conjugation reaction between gold nanoparticles and radiolabeled cetuximab was assessed using electrophoresis gel (10% SDS–PAGE gel, under nonreducing conditions), followed by a radio-TLC analysis. Thermogravimetric analysis were performed with a TGA Q500 instrument (TA instruments, Italy) to evaluate AuNPs–PPAA–cetuximab–^{89}Zr composition as previously reported (22). A cell-based ELISA was achieved to assess the relative binding affinity. In addition, phosphorylation assays and subsequent western blot analysis were carried out to control the preservation of the cetuximab ability to inhibit the EGF-induced phosphorylation of EGFR after its conjugation to nanoparticles (22).

4.4. *In vitro* stability of radioimmunoconjugates in storage solution and in plasma

Chemical stability of purified ^{89}Zr–Df–Bz–NCS–cetuximab and AuNPs–PPAA–cetuximab–^{89}Zr in a solution of 5 mg ml^{-1} gentisic acid in 0.25 M sodium acetate, pH 5.4–5.6, was checked in storage conditions at 4 °C. Samples were drawn at regular time points and the proportion of free ^{89}Zr was analyzed by radio-TLC. In these conditions, the release of free ^{89}Zr was lower than 20%, 2 weeks after labeling reaction.

In vitro plasmatic stability of both ^{89}Zr–Df–Bz–NCS–cetuximab and AuNPs–PPAA–cetuximab–^{89}Zr was studied in fresh mouse plasma, by incubating the solution of radiolabeled antibodies (1:2 v/v dilution at a final concentration of 1.6 MBq ml^{-1}; sodium azide added to 0.02%) at 37 °C with stirring. At different time points (6, 24, 48, 72 and 96 h), aliquots of plasma (10 μl) were analysed using radio-ITLC and this showed that ^{89}Zr was slightly dissociated from the antibody over time. Starting from a solution without free ^{89}Zr (100% purity), the percentages of dissociation were <5% after 6 h, 10% after 24 h, 15% after 48 h and 20% after 72 and 96 h, for both radioimmunoconjugates.

4.5. Comparative biodistribution studies in mice using animal-PET imaging

For the biodistribution and PET studies, NMRI male nude mice (32–37 g, 5–7 weeks old; Janvier, France) bearing human epithelial carcinoma xenografts (A431) were used. A431 cancer cell line was maintained in appropriate medium Dulbecco's modified Eagle's medium (glucose 4.5 g l^{-1} without pyruvate, Gibco-Invitrogen, Belgium), supplemented with 10% heat inactivated fetal bovine serum (Gibco-Invitrogen, Belgium) and 1% streptomycin–penicillin (Gibco-Invitrogen, Belgium). A431 cells (10×10^6) were inoculated subcutaneously into flanks of NMRI nude mice (two tumors per mouse). Mice were used for *in vivo* experiments when the diameter of tumors reached 7–8.5 mm. All animal experiments were conducted in accordance with national and university animal care regulations.

To compare the pharmacokinetic behavior of radiolabeled antibody conjugated to gold nanoparticles and uncoupled radiolabeled antibody, two groups of three to five mice were injected intravenously into the lateral tail vein with either freshly prepared ^{89}Zr–Df–Bz–NCS–cetuximab or with AuNPs–PPAA–

cetuximab–^{89}Zr, (3.3–4.6 MBq, total of 200–350 μg mAb per mouse). Additionally, to assess the *in vivo* specificity of cetuximab-conjugated gold nanoparticles, a group of three A431 tumor-bearing mice (blocking group, one tumor per mouse) was injected with an excess of unlabeled cetuximab (2 mg mAb per mouse) 2 h before the injection of AuNPs–PPAA–cetuximab–^{89}Zr (2.2-3.5 MBq, total of 200 μg mAb per mouse) as previously described (36). The blocking group was compared with the group of mice who received only AuNPs–PPAA–cetuximab–^{89}Zr without a saturating dose.

PET imaging was performed using a dedicated small-animal PET scanner (MOSAIC, Philips Medical Systems; Cleveland, USA) with a spatial resolution of 2.5 mm (full width at half maximum) (37). Mice were imaged under anesthesia by inhalation of 1.5% isoflurane (Abbott Laboratories, Belgium)–oxygen gas mixture (2 l min^{-1}). The PET acquisitions were carried out with an energy window of 410–660 keV. Static acquisitions were performed at different time points (6, 24, 48, 72, 96 and 168 h after tracer injection). For emission scans, acquisition time was adapted to compensate for decay in order to ensure significant statistics. Before reconstruction, raw data were corrected for random and scattered coincidences, as well as for system dead time. For attenuation correction of emission data, transmission scans were acquired using a 370 MBq ^{137}Cs source. All images were reconstructed with a fully 3D iterative algorithm (3D-RAMLA). The reconstructed matrix consisted of 120 transverse images of 128×128 voxels, with a voxel size of 1 mm^3.

4.6. PET data analyses

PET data were analyzed using PMOD software (PMOD™, version 3.3, PMOD Technologies Ltd, Zurich, Switzerland). Regions of interest (ROIs) were delineated after image normalization. An empirically determined system calibration factor for mice was used to convert the ROI value (counts per pixel per minute) to activity concentration (nCi ml^{-1}). Image scale was first corrected according to the PET calibration factor, including the positron branching ratio, the physical decay to the time of injection, the acquisition period and the injected dose. This normalization was used to parameterize images in terms of percentage of the injected dose per milliliter.

The 2D ROIs were established on consecutive transversal slices using a 50% isocontour tool (ROI including the pixel values greater than 50% of the maximum pixel) that semiautomatically defined a 3D volume of interest around the tissue of interest. The tracer uptake was assessed in liver and tumors. Moreover, a background region was drawn in the pelvic region. The same background volume was applied for all animal analyses and it was representative for tissues with low nonspecific uptake. The tumor uptake was also expressed as tumor-to-background ratio, calculated as the mean activity in tumor region divided by the mean activity obtained in the background region.

4.7. Statistical analysis

Results are given as means ± SEM values from n animals. Data calculations were performed with Prism software (Graph Pad™ Software Inc., version 5.02). The differences in tissue uptake between two groups were considered significant if the *p*-values from unpaired *t*-tests were ≤0.05 (*), ≤0.01 (**) or ≤ 0.001 (***). The differences in tissue uptake at different time points were assessed by the one-way analysis of variance and Tukey *post-hoc* test.

Supporting Information

Supporting information can be found in the online version of this article.

Acknowledgments

REFERENCES

1. Bharali DJ, Mousa SA. Emerging nanomedicines for early cancer detection and improved treatment: current perspective and future promise. Pharmacol Ther 2010;128:324–335.
2. Mallidi S, Larson T, Aaron J, Sokolov K, Emelianov S. Molecular specific optoacoustic imaging with plasmonic nanoparticles. Opt Express 2007;15:6583–6588.
3. Glaser ES, Massey KL, Zhu C, Curley SA. Pancreatic carcinoma cells are susceptible to noninvasive radio frequency fields after treatment with targeted gold nanoparticles. Surgery 2010;148:319–324.
4. Tiwari PM, Vig K, Dennis VA, Singh R. Functionalized gold nanoparticles and their biomedical applications. Nanomaterials 2011;1:31–63; doi: 10.3390/nano1010031
5. Fay F, Scott CJ. Antibody-targeted nanoparticles for cancer therapy. Immunotherapy 2011;3:381–394.
6. Mendelsohn J, Baselga J. Epidermal growth factor receptor targeting in cancer. Semin Oncol 2006;33:369–385.
7. Li S, Schmitz KR, Jeffrey PD, Wiltzius JJ, Kussie P, Ferguson KM. Structural basis for inhibition of the epidermal growth factor receptor by cetuximab. Cancer Cell 2005;7:301–311.
8. Tejani MA, Cohen RB, Mehra R. The contribution of cetuximab in the treatment of recurrent and/or metastatic head and neck cancer. Biologics 2010;4:173–185; PMID: 20714355
9. Fakih M, Wong R. Efficacy of the monoclonal antibody EGFR inhibitors for the treatment of metastatic colorectal cancer. Curr Oncol 2010;17 suppl 1:S3–17.
10. El-Sayed IH, Huang X, El-Sayed MA. Selective laser photo-thermal therapy of epithelial carcinoma using anti-EGFR antibody conjugated gold nanoparticles. Cancer Lett 2006;239:129–135.
11. Sokolov K, Follen M, Aaron J, Pavlova I, Malpica A, Lotan R, Richards-Kortum R. Real-time vital optical imaging of precancer using anti-epidermal growth factor receptor antibodies conjugated to gold nanoparticles. Cancer Res 2003;63:1999–2004.
12. Kah JCY, Olivo MC, Lee CGL, Sheppard CJR. Molecular contrast of EGFR expression using gold nanoparticles as a reflectance-based imaging probe. Mol Cell Probes 2008;22:14–23.
13. El-Sayed IH, Huang X, El-Sayed MA. Surface Plasmon resonance scattering and absorption of anti-EGFR antibody conjugated gold nanoparticles in cancer diagnostics: application in oral cancer. Nano Lett 2005;5:829–834; doi: 10.1021/nl050074e
14. Sonavane G, Tomoda K, Makino K. Biodistribution of colloidal gold nanoparticles after intravenous administration: effect of particle size. Colloids Surf B Biointerfaces 2008;66:274–280.
15. Schroeder A, Heller DA, Winslow MM, Dahlman JE, Pratt GW, Langer R, Jacks T, Anderson DG. Treating metastatic cancer with nanotechnology. Nat Rev Cancer 2012;12:39–50; doi: 10.1038/nrc3180
16. Vugts DJ, van Dongen GAMS. ^{89}Zr-labeled compounds for PET imaging guided personalized therapy. Drug Discov Today Technol 2011;8:e53–e61; doi: 10.1016/j.ddtec.2011.12.004.
17. Meijs WE, Haisma HJ, Klok RP, van Gog FB, Kievit E, Pinedo HM, Herscheid JD. Zirconium-labeled monoclonal antibodies and their distribution in tumor-bearing nude mice. J Nucl Med 1997;38:112–118.
18. Dijkers ECF, Kosterink JGW, Rademaker AP, Perk LR, van Dongen GAMS, Bart J, de Jong JR, de Vries EG, Lub-de Hooge MN. Development and characterization of clinical-grade Zr-89-trastuzumab for HER2/neu immunoPET imaging. J Nucl Med 2009;50:974–981; doi: 10.2967/jnumed.108.060392
19. Borjesson PK, Jauw YW, Boellaard R, de Bree R, Comans EF, Roos JC, Castelijns JA, Vosjan MJ, Kummer JA, Leemans CR, Lammertsma AA, van Dongen GA. Performance of immuno-positron emission tomography with zirconium-89-labeled chimeric monoclonal antibody U36 in the detection of lymph node metastases in head and neck cancer patients. Clin Cancer Res 2006;12:2133–2140.
20. Borjesson PKE, Jauw YWS, de Bree R, Roos JC, Castelijns JA, Leemans CR, van Dongen GA, Boellaard R. Radiation dosimetry of zirconium-89-labeled chimeric monoclonal antibody U36 as used for immuno-PET in head and neck cancer patients. J Nucl Med 2009;50:1828–1836.
21. van Dongen GAMS, Visser GWM, Lub-de-Hooge MN, De Vries EG, Perk LR. Immuno-PET: A navigator in monoclonal antibody development and applications. Oncologist 2007;12:1379–1389.
22. Marrega R, Karmani L, Flamant L, Nageswaran PG, Valembois V, Masereel B, Feron O, Vander Borght T, Lucas S, Michiels C, Gallez B and Bonifazi D. Antibody-functionalized polymer-coated gold nanoparticles targeting cancer cells: an in vivo and in vitro study. J Mater Chem 2012;22:21305–21312.
23. Thorek DLJ, Elias DR and Tsourkas A. Comparative analysis of nanoparticle-antibody conjugations: carbodiimide versus click chemistry. Mol Imag 2009;8:221–229.
24. van Gog FB, Visser GWM, Klok RP, van der Schors R, Snow GB, van Dongen GAMS. Monoclonal antibodies labeled with rhenium-186 using the MAG3 chelate: relationship between the number of chelated groups and biodistribution characteristics. J Nucl Med 1996;37:352–362.
25. Kukis DL, DeNardo GL, DeNardo SJ, Mirick GR, Miers LA, Greiner DP, Meares CF. Effect of the extent of chelate substitution on the immunoreactivity and biodistribution of 2IT-BAT-Lym-1 immunoconjugates. Cancer Res 1995;55:878–884.
26. Tinianow JN, Gill HS, Ogasawara A, Flores JE, Vanderbilt AN, Luis E, Vandlen R, Darwish M, Junutula JR, Williams SP, Marik J. Site-specifically Zr-89-labeled monoclonal antibodies for ImmunoPET. Nucl Med Biol 2010;37:289–297.
27. Mealey Jr J. Turn-over of carrier-free zirconium-89 in man. Nature 1957;179:673–674; doi: 10.1038/179673a0
28. Abou DS, Ku T, Smith-Jones PM. In vivo biodistribution and accumulation of ^{89}Zr in mice. Nucl Med Biol 2011;38:675–681.
29. Moreau N, Michiels C, Masereel B, Feron O, Gallez B, Vander Borght T, Lucas S. PVD synthesis and transfer into water-based solutions of functionalized gold nanoparticles. Plasma Process Polymer 2009;6: S888–S892; doi: 10.1002/ppap.200932210
30. Holland JP, Sheh YC, Lewis JS. Standardized methods for the production of high specific-activity zirconium-89. Nucl Med Biol 2009;36:729–739.
31. Kandil SA, Scholten B, Saleh ZA, Youssef AM, Qaim SM, Coenen HH. A comparative study on the separation of radiozirconium via ion-exchange and solvent extraction techniques, with particular reference to the production of ^{88}Zr and ^{89}Zr in proton induced reactions on yttrium. J Radioanal Nucl Chem 2007;274:45–52; doi: 10.1007/s10967-006-6892-2
32. Verel I, Visser GWM, Boellaard R, Stigter-van Walsum M, Snow GB, van Dongen GAMS. ^{89}Zr immuno-PET: Comprehensive procedures for the production of ^{89}Zr-labeled monoclonal antibodies. J Nucl Med 2003;44:1271–1281.
33. Vosjan MJWD, Perk LR, Visser GW, Budde M, Jurek P, Kiefer GE, van Dongen GA. Conjugation and radiolabeling of monoclonal antibodies with zirconium-89 for PET imaging using the bifunctional chelate p-isothiocyanatobenzyl-desferrioxamine. Nat Prot 2010;5:739–743.
34. Perk LR, Vosjan MJWD, Visser GW, Budde M, Jurek P, Kiefer GE, van Dongen GA. p-Isothiocyanatobenzyl-desferrioxamine: a new bifunctional chelate for facile radiolabeling of monoclonal antibodies with zirconium-89 for immuno-PET imaging. Eur J Nucl Med Mol Imag 2010;37:250–259.
35. Masereel B, Dinguizli M, Bouzin C, Moniotte N, Feron O, Gallez B, Vander Borght T, Michiels C, Lucas S. Antibody immobilization on gold nanoparticles coated layer-by-layer with polyelectrolytes. J Nanopart Res 2011;13:1573–1580.
36. Hong H, Yang Y, Zhang Y, Engle JW, Barnhart TE, Nickles RJ, Leigh BR, Cai W. Positron emission tomography imaging of CD105 expression during tumor angiogenesis. Eur J Nucl Med Mol Imag 2011;38:1335–1343.
37. Huisman MC, Reder S, Weber AW, Ziegler SI, Schwaiger M. Performance evaluation of the Philips MOSAIC small animal PET scanner. Eur J Nucl Med Mol Imag 2007;34:532–540.